Received: 23 July 2022 | Revised: 9 October 2022 | Accepted: 22 November 2022

DOI: 10.1002/rnc.6526

RESEARCH ARTICLE

WILEY

Robust fractional-order fast terminal sliding mode control with fixed-time reaching law for high-performance nanopositioning

Geng Wang[1,2] | **Yongsheng Zhou**[2] | **Lei Ni**[1] | **Sumeet S. Aphale**[3]

[1]Key Laboratory of Testing Technology for Manufacturing Process of Ministry of Education, Southwest University of Science and Technology, Mianyang, People's Republic of China

[2]School of Mechanical and Power Engineering, Henan Polytechnic University, Jiaozuo, People's Republic of China

[3]Artificial intelligence, Robotics and Mechatronic Systems Group (ARMS), School of Engineering, University of Aberdeen, Aberdeen, UK

Correspondence
Sumeet S. Aphale, Artificial intelligence, Robotics and Mechatronic Systems Group (ARMS), School of Engineering, University of Aberdeen, Aberdeen AB243UE, UK.
Email: s.aphale@abdn.ac.uk

Funding information
China Scholarship Council, Grant/Award Number: 201908410107; National Natural Science Foundation of China, Grant/Award Number: 51505133

Abstract

For high-performance trajectory tracking at the nanometer scales, this paper presents a new fast terminal sliding mode controller, which combines a recursive integer-order non-singular high-order sliding manifold and a fractional-order fast fixed-time reaching law to ensure globally fast convergence, and adopts a time-delay-estimation (TDE) based disturbance estimator deeming the designed controller robust to parameter uncertainty. Stability of the designed controller is verified through the Lyapunov framework, where the full analyses of convergence region and settling time are also presented. The tracking performance is experimentally verified on a piezo-stack driven nano-positioning platform. To showcase the performance improvements, measured closed-loop performance of the proposed controller is contrasted with those obtained using three benchmark control approaches namely the basic Proportional-Integral-Derivative (PID), the popular Positive Position Feedback with Integral action (PPF+I), and the traditional linear sliding mode controller (LSMC).

KEYWORDS

fast fixed-time convergence, fractional calculus, high-order sliding mode, nanopositioning, time delay estimation

1 | INTRODUCTION

In recent years, piezo-actuated nanopositioners have found widespread application in several micro/nanoscale hi-tech systems such as atomic force microscopy,[1] nanolithography,[2] microinjection systems,[3] and fast tool servo mechanisms.[4] This is mainly due to the ease of operation and system integration, mechanical robustness, repeatability, high-resolution and design simplicity afforded by piezo-actuated stages; with further performance enhancements made possible by advances in control technology.[5-7] The positioning performances of the piezoelectric stages are usually restricted by the inherent hysteresis,[8-10] creep, lowly-damped resonance modes, and parameter uncertainties. Feedback control methods

can ensure robustness in presence of system parameter uncertainties, and enhance the transient and steady-state performance of the system appropriately. Usually, for piezo-actuated nanopositioners, these methods focus on mitigating the adverse effects of resonant linear dynamics, inherent nonlinearities, model uncertainty, and external disturbance, on the steady-state precision and achievable positioning bandwidth. Consequently, a significant volume of literature focuses on hysteresis modeling and inverse control methods.[11-13] The key drawback of these techniques lie in the inevitable error in modeling and parameter identification. Consequently, these techniques are often combined with other feedback control methods, such as proportional–integral–derivative (PID) control,[14] sliding-mode control,[15,16] model predictive control,[17] and so forth, to deliver adequate performance.

The sliding-mode control (SMC) is a popular nonlinear control method that has recently gained wide-spread attention due to its effectiveness and robustness to disturbances.[18,19] The core concept of the SMC is to keep system state sliding on a specifically designed manifold that guarantees predefined (desired) dynamic performance. The traditional linear SMC method can only guarantee the asymptotic stability of the closed-loop system.[20,21] Consequently, persistent control input is needed to guarantee asymptotic stability.[22,23] On the other hand, external control inputs are not needed if a system is finite-time stable,[24-27] which means the system can reach a stable operating point within a finite settling time. Thus, in many engineering applications, finite-time stability[28] is highly desirable. In case of nanopositioners, finite-time stability can significantly improve the speed (bandwidth) of the nanopositioning system. The nonlinear sliding surface based SMC, also known as the terminal sliding-mode control (TSMC), has been developed to possess this property.[29] However, TSMC may lead to chattering issues,[30] singularity,[31] and slower convergence speed when compared to linear SMC, if the system is operating far away from the equilibrium point.[3,32] On the other hand, the state trajectories of TSMC control systems with finite-time stability exhibit high amplitudes[33,34] and long convergence times.[35] Furthermore, for TSMC schemes, convergence time is highly dependent on the initial conditions and strictly increases with increase in initial conditions of the system. To address this issue, a fixed-time stability method, in which the settling time of a stable system is fixed and independent of the initial system state has also been proposed.[36] However, these advances have to date, not been applied to nanopositioning systems in order to explore the possible performance improvements they can afford.

Fractional calculus has recently become very attractive in several engineering applications.[37-40] It has also been proved that the fractional integral sliding surface is equivalent to a low-pass filter on the sign function and thus can eliminate high-frequency components–typically the cause of instability with the potential to excite unmodeled high-frequency system dynamics.[41] Fractional-order (FO) control systems[42-44] can provide more adjustable degrees of freedom than its Integer-order (IO) counterparts. Some recent studies[10,45] also show the superiority of FO controller over IO designs. In 2020, a continuous fractional-order nonsingular terminal sliding mode controller[46] is proposed for a class of second-order nonlinear systems. For the speed operation of permanent magnet synchronous motor, an adaptive super-twisting Fractional-order PID sliding mode controller[47] is proposed based on an extended state observer. It's worth noting that the fusion of fractional calculus and fixed-time sliding mode control could be an effective way to improve the performance of several engineering systems. In literature,[48] a fixed-time fractional-order sliding mode controller is proposed and it can effectively stabilize a nonlinear power system. Junkang[49] proposed a fast fixed-time nonsingular terminal sliding mode controller which is applied to chaos suppression in power systems. However, There is no relevant report on fractional fixed-time sliding mode control applied to piezoelectric driven high precision positioning system to the best of authors' knowledge. As fixed convergence time is more attractive than finite time for the practical application, the fixed-time sliding mode control method based on fractional calculus remains a challenge to be explored for piezoelectric-actuated positioning system, which is the main motivation of this paper.

As analyzed above, TSMC control schemes with fixed convergence time is highly desirable because the settling time is independent of the initial system state. However, the fixed-time SMC based on fractional calculus remains a challenge to be explored. In addition, the needs of designing high performance controller for piezoelectric positioner with high-order model can be satisfied. The benefits of this study include but are not limited to that the following academic questions can be solved so as to realize high performance positioning for piezoelectric positioner.[50,51] For example, how to combine high order sliding mode and fractional calculus to design a robust, stable, non-singular, global fast convergent controller? How to ensure its stability, even fixed time stability? How to calculate the time of its stability?

Bearing the above questions in mind, out main focus in this paper is to address fixed-time high precision tracking problem for a high-order nonlinear system based on high-order sliding mode and fractional calculus. In this work, a robust high-order sliding mode control method based on a recursive high-order sliding manifold aimed at positioning performance improvement of a piezoelectric platform is proposed. The controller combines a recursive high-order

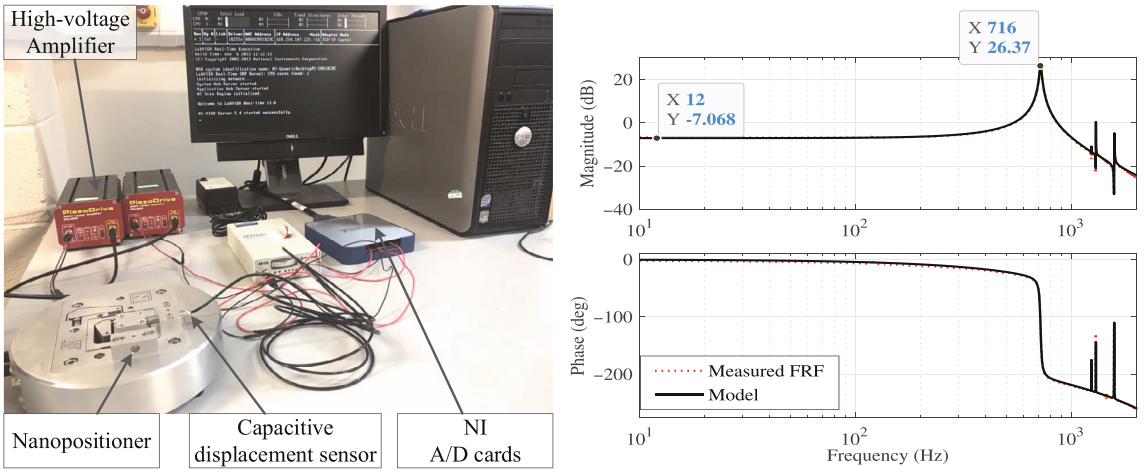

FIGURE 1 (A) The experimental setup used in this work showing the two-axis, serial kinematic, piezoelectrically actuated nanopositioner, the high-voltage amplifiers, the capacitive displacement sensor, and the computer embedded with NI A/D cards and LabView. (B) Measured magnitude response of the system (· · ·) and the magnitude response of the full linear model (—) adopted in this work showing excellent acuracy in capturing the linear in-bandwidth dynamics.

sliding manifold, a fractional order fast fixed-time reaching law and a time-delay-estimation (TDE) disturbance estimation method. The major contributions of this work are highlighted as follows:

1. A piezoelectric platform is accurately modelled, including a linear high-order (10th) component, a nonlinear Bouc-Wen-type hysteresis component, and a lumped TDE disturbance.
2. A new practical robust fractional-order terminal sliding mode control method is synthesized by combining a recursive high-order sliding manifold, a modified fractional-order fast fixed-time reaching law and a TDE disturbance estimation methodology.
3. With the aid of the model-free nature of TDE, the controller is capable of adequately compensating for the residual uncompensated hysteresis and unmodeled dynamics.
4. The stability of the proposed controller, convergence region and settling time of system state are theoretically proved via Lyapunov theory.
5. The excellent performances of the proposed controller in terms of high tracking accuracy, fast convergence, non-singularity, robustness, chattering-free have been verified by comparing the experimental results with basic PID, the popular PPF+I and the traditional linear LSMC controllers.

In order to clearly demonstrate the controller design, analysis, and experimental process and results for the piezoelectric platform, the rest of this paper is logically organized as follows. Section 2 introduces the controlled plant (piezoelectric platform) and the entire experimental system, and presents the accurate modeling process of the controlled plant including linear dynamics part and nonlinear hysteresis part. Then, the controller synthesis is presented in detail in Section 3 which consists of *Mathematical foundations*, *Inverse model of hysteresis*, *TDE disturbance estimation*, and *Sliding mode based controller design*. Next, the stability and convergence property are analysed in Section 4. Section 5 gives out the experimental settings, tracking results, and performance analysis. Finally, the paper is concluded in Section 6.

2 | SYSTEM MODELING OF THE PLATFORM

This section first describes the experimental setup employed in this work. It then describes the complete system identification and modeling process resulting in a model that encapsulates the linear dynamics as well as the nonlinear hysteresis. This model is subsequently employed during the control design and simulations. Experiments are carried out directly on the setup shown in Figure 1 using the hardware described below.

2.1 | Experimental setup description

The experimental setup used in this work is shown in Figure 1A. It consists of a piezo-stack actuated, flexure-guided, two-axis ($x - y$) nanopositioner. Each axis of the nanopositioner is driven by a 10 mm, 200 V piezoelectric stack actuator capable of producing 40 μm motion along each axis. The nanopositioner also provides integrated mounts for capacitive sensor probes. The MicroSense 6810 capacitive displacement sensor and 6504-01 probe with a sensitivity of 5 mm/V provides a voltage signal proportional to the displacement sensed along each axis. The piezoelectric stack actuators are supplied with both AC actuation and DC bias voltages by two PiezoDrive PDL200 voltage amplifiers with a gain of 20.

2.2 | Modeling the platform

Before designing a controller, the model of the piezoelectric platform must be established. In this work, one axis of the piezo-actuated nanopositioner is employed so as to demonstrate the efficacy of the proposed control scheme. Firstly, the linear dynamics of the platform is modeled as a general time-domain differential equations:

$$y^{(n)}(t) + \sum_{k=0}^{n-1} a_k y^{(k)}(t) = \sum_{k=0}^{m} b_k u^{(k)}(t) \tag{1}$$

where $u(t)$ is the input voltage applied to the platform as a function time t; $y(t)$ is the displacement produced along the axis; $u^{(k)}(t)$ and $y^{(k)}(t)$ are respectively the kth derivatives of $u(t)$ and $y(t)$; m and n are the orders of the model, and $m < n$; a_k and b_k are constant coefficients of the model.

In order to aquire the coefficients and orders of the above model, the dynamics of one axis of the nanopositioner is identified by applying a sinusoidal chirp signal (from 10 to 1500 Hz) with an amplitude of 0.2 V as input to the voltage amplifier of the x-axis and measuring the output signal (sensor voltage proportional to axial displacement) along the x axis.Then, the small signal frequency response functions (FRFs) is computed by taking the fourier transform of the recorded data. The recorded frequency response clearly shows that the dynamics within the recorded bandwidth-of-interest are dominated by a lowly-damped resonant mode that occurs at 716 Hz. To validate the identified model, the magnitude response of the identified model was superimposed on the measured magnitude response of the nanopositioner's axis, see Figure 1B. Clearly, the identified model is a very accurate match to the measured linear dynamics of the nanopositioner axis. It is worth noting that the order n in Equation (1) is set to 10, which means the controlled platform is a high-order plant.

Secondly, the inherent hysteresis nonlinear behaviour of the piezo-stack actuator employed by the nanopositioner is usually modeled by a hysteresis model. Due to its apparent simplicity, its ability to capture the nonlinear behavior accurately and its popularity, the Bouc-Wen model is often adopted in the literatures and can be generally expressed as follows:[52]

$$\begin{cases} H(t) = du - h \\ \dot{h} = \alpha_1 \dot{u} - \alpha_2 |\dot{u}| h - \alpha_3 \dot{u} |h| \end{cases} \tag{2}$$

where $H(t)$ is an immeasurable hysteresis displacement; d is piezoelectric constant; h is an intermediate state variable whose time derivative is $\dot{h}$; α_1, α_2 and α_3 are the coefficients that determine the shape and orientation of the hysteresis loop.

Thirdly, all the other unmodeled dynamics and uncertainties can be considered as a lumped disturbance.

Combining the above three aspects, the entire dynamic model of one axis of the nanopositioner can be expressed as:

$$y^{(n)}(t) + \sum_{k=0}^{n-1} a_k y^{(k)}(t) + H(t) + \Delta(t) = \sum_{k=0}^{m} b_k u^{(k)}(t) \tag{3}$$

where $\Delta(t)$ is the uncertain displacement caused by the lumped disturbance including all the un-modelled (out-of-bandwidth) linear and nonlinear dynamics and other disturbances from temperature variation and aging and so on.

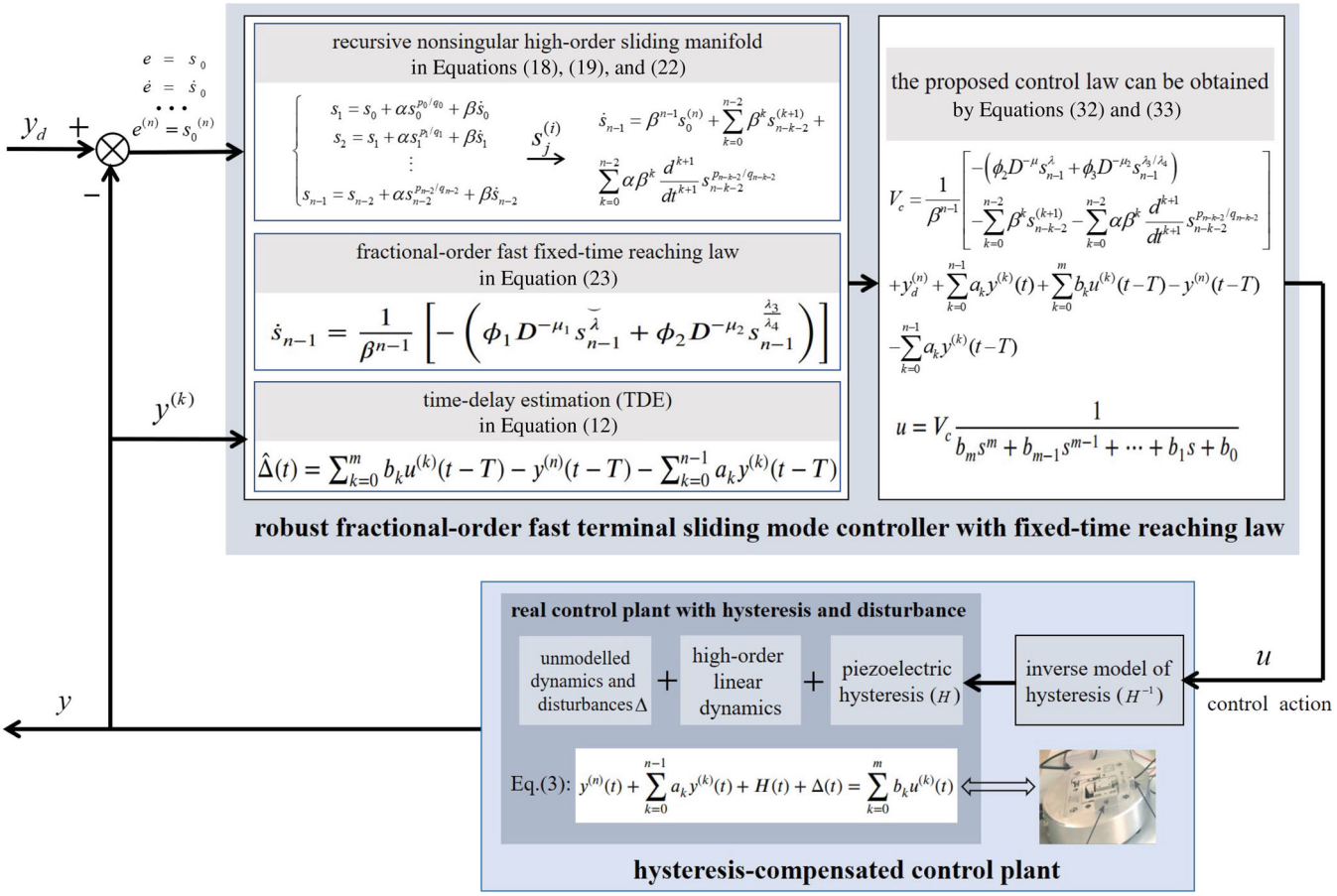

FIGURE 2 Block-diagram of the proposed control scheme showing the overall signal flow

3 | CONTROLLER SYNTHESIS

In this section, a robust fractional-order fast terminal sliding mode scheme with fixed-time convergence law is proposed for controlling the above-mentioned platform. The control objective is to track a scanning trajectory (typically triangular in nature) accurately in the presence of unknown disturbances. Firstly, a hysteresis compensation scheme based on Bouc-Wen model is employed in order to eliminate hysteretic nonlinearity in advance. Then, with the hysteresis-compensated plant which can be quite accurately approximated by a high-order linear dynamical systems with uncertainties, we proposed a feedback sliding mode control scheme which combines a recursive high-order sliding manifold, a fractional-order fast fixed-time reaching law and a time-delay estimation. The block diagram of the control system is shown in Figure 2.

3.1 | Mathematical foundations

Definition 1 [53]: The α th-order Reimann-Liouville fractional integration of function $f(t)$ with respect to t is given by the following

$$ {}_{t_0}I_t^{\alpha} f(t) = \frac{1}{\Gamma(\alpha)} \int_{t_0}^{t} \frac{f(\tau)}{(t-\tau)^{1-\alpha}} \mathrm{d}\tau \tag{4} $$

where $\Gamma(\alpha)$ is the gamma function and t_0 is the initial time.

Definition 2 [53]: The α th-order Reimann-Liouville fractional derivative of of function $f(t)$ with respect to t is defined as follows

$$ {}_{t_0}D_t^{\alpha} f(t) = \frac{\mathrm{d}^{\alpha} f(t)}{\mathrm{d}t^{\alpha}} = \frac{1}{\Gamma(m-\alpha)} \frac{\mathrm{d}^m}{\mathrm{d}t^m} \int_{t_0}^{t} \frac{f(\tau)}{(t-\tau)^{\alpha-m+1}} \, \mathrm{d}\tau \tag{5} $$

where $m-1 < \alpha \leq m, m \in N$.

Lemma 1 (54). *Fractional-order differentiation is linear; if A, B are constants, then*

$$ {}_0D_t^{\alpha}[Af(t) + Bg(t)] = A\,{}_0D_t^{\alpha} f(t) + B\,{}_0D_t^{\alpha} g(t) \tag{6} $$

$$ {}_0D_t^{\alpha}[-f(t)] = -{}_0D_t^{\alpha} f(t) \tag{7} $$

Lemma 2 (55). *For $\mu > 0, v > 0$, the FO calculus of function $f(t) = (t-a)^v$ is*

$$ {}_aD_t^{-\mu} f(t) = \frac{(t-a)^{v+\mu}}{\Gamma(\mu)} B(\mu, v+1) \tag{8} $$

where $B(\mu, v)$ is the beta function, and $\Gamma(\mu)$ is the gamma function.

Lemma 3 (41,56). *Consider the following system*:

$$ \dot{x}(t) = -ax^{\mu_1} - bx^{\mu_2}, x(0) = x_0 \tag{9} $$

where $a, b > 0$, and μ_1, μ_2 are the ratio of two positive odd integers which satisfying $\mu_1 > 1$ and $\mu_2 < 1$. Then, the equilibrium point of system (3) is fixed-time stable, and the settling time is upper bounded by:

$$ T < \frac{1}{a\,(\mu_1 - 1)} + \frac{1}{b\,(1-\mu_2)} \tag{10} $$

It should be noted that, in this work the fractional order term is approximated by the Oustaloup refined filter method.[57] And, the notation $D^{-\alpha}$ and D^{α} respectively indicate the Reimann-Liouville fractional integration and derivative with the interval from t_0 to t.

3.2 | Inverse model of hysteresis

In the hysteresis compensation scheme, the inverse hysteresis based on Bouc-Wen model is employed, which is similar to the method proposed in literature.[58] The main idea is shown in Figure 3, which shows that the hysteresis compensation scheme in series of inverse model and Bouc-Wen model can linearize the hysteresis nonlinearity of the system.

The specific process is as follows. (1) The Bouc-Wen hysteresis model is identified by a differential evolution algorithm,[59] and then the corresponding parameters in formula (2) can be obtained. (2) With the second equation in expression (2), the term $\int \dot{h}(\cdot)$ in Figure 3 can be constructed. (3) According to Equation (2), the output of the inverse hysteresis model can be designed as $\frac{1}{d}(input + h)$, where h can be calculated by Equation (2). As this is a very mature scheme, interested readers can consult the literature[58] for more details.

3.3 | TDE disturbance estimation

After the hysteresis compensation, the entire dynamic model of one axis of the nanopositioner can be approximated by:

$$ y^{(n)}(t) + \sum_{k=0}^{n-1} a_k y^{(k)}(t) + \Delta(t) = \sum_{k=0}^{m} b_k u^{(k)}(t) \tag{11} $$

As demonstrated above, the term $\Delta(t)$ is complicated and can not be easily obtained. Thus, the value of $\Delta(t)$ is estimated with the time-delayed method in this work when designing the feedback controller. With the disturbance estimation

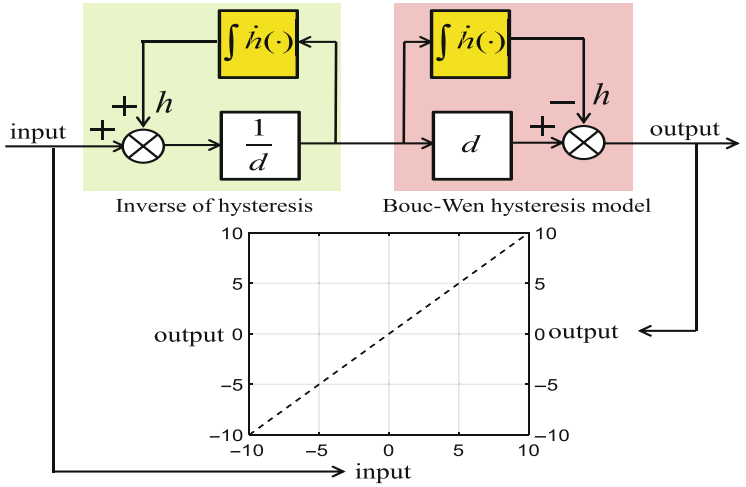

FIGURE 3 The principle of inverse-hysteresis compensation scheme based on Bouc-Wen model.

technique,[60,61] the estimation value of disturbance $\Delta(t)$ can be defined as follows:

$$\hat{\Delta}(t) \triangleq \Delta(t-T) = \sum_{k=0}^{m} b_k u^{(k)}(t-T) - y^{(n)}(t-T) - \sum_{k=0}^{n-1} a_k y^{(k)}(t-T) \tag{12}$$

where T is the sampling interval and usually is a very small value. Then the controlled plant (11) becomes:

$$y^{(n)}(t) + \sum_{k=0}^{n-1} a_k y^{(k)}(t) + \hat{\Delta}(t) + \tilde{\Delta}(t) = \sum_{k=0}^{m} b_k u^{(k)}(t) \tag{13}$$

where $\tilde{\Delta}(t)$ is the estimation error and can be defined as:

$$\tilde{\Delta}(t) = \Delta(t) - \hat{\Delta}(t) \tag{14}$$

Usually, we suppose the estimation error $\tilde{\Delta}(t)$ is bounded and satisfies

$$|\tilde{\Delta}(t)| < \bar{\tilde{\Delta}} \tag{15}$$

where $\bar{\tilde{\Delta}}$ is the upper bound of estimation error $\tilde{\Delta}$.

Remark 1. In this work, the employment of TDE estimator is mainly considered from the practical point of view. The basic idea of the TDE estimation is to voluntarily introduce a small delay and then to use past observations regarding both inputs and responses to compensate the unknown dynamics and disturbances simultaneously. The advantages of using the TDE estimation method include (1) The TDE estimation only acquire the residual system dynamics with just time-delayed system information (residual dynamics are not needed to be modelled any more) and ensures a fascinating model-free scheme. (2) The shorter the TDE sampling interval, the more accurate the disturbance estimation. In this work, the sampling frequency is 20 kHz, which means the sampling interval is small enough to get a sufficient tracking accuracy. (3) The TDE estimation is essentially an online estimation method, and thus it can real-time compensate for the uncertainties or the disturbances, which is very preferable in the practical application.

3.4 | Sliding mode based controller design

This control design begins with the design of a recursive high-order sliding manifold which is then followed by proposing a new fractional-order fast fixed-time reaching law.

3.4.1 | Recursive high-order sliding manifold

Define position tracking error:

$$e = y - y_d \tag{16}$$

where y is the output displacement, and y_d is the desired displacement command.

Then, we have the all the derivatives of the tracking error

$$e^{(i)} = y^{(i)} - y_d^{(i)}, (i = 1, 2, \ \dots \ n) \tag{17}$$

Let

$$s_0 = e, \quad \dot{s}_0 = \dot{e}, \quad \dots, \quad s_0^{(n)} = e^{(n)} \tag{18}$$

A recursive high-order fast terminal sliding manifold is defined as follows:

$$\begin{cases} s_1 = s_0 + \alpha s_0^{p_0/q_0} + \beta \dot{s}_0 \\ s_2 = s_1 + \alpha s_1^{p_1/q_1} + \beta \dot{s}_1 \\ s_3 = s_2 + \alpha s_2^{p_2/q_2} + \beta \dot{s}_2 \\ \vdots \\ s_j = s_{j-1} + \alpha s_{j-1}^{p_{j-1}/q_{j-1}} + \beta \dot{s}_{j-1} \\ s_{n-1} = s_{n-2} + \alpha s_{n-2}^{p_{n-2}/q_{n-2}} + \beta \dot{s}_{n-2} \end{cases} \tag{19}$$

where $\alpha, \beta \in \mathrm{R}^+$; p_j, q_j are all constant positive odd number, $j = 1, 2, \ \dots \ , n-1$; $n - 1 < \frac{p_{j-1}}{q_{j-1}} < n$. It should be noted that $n \geq 2$ means $\frac{p_{j-1}}{q_{j-1}} > 1$. This can ensure that we don't have zero denominators in the derivation calculations and thus can guarantee the non-singularity property. Using the same calculation method as in the literature,[62,63] we have the definition: $s^{p/q} \triangleq |s|^{p/q}\mathrm{sign}(s)$, which always returns a smooth, monotonically increasing real function. Note that sign$(\cdot)$ means the sign function.

From formula (19) we can get:

$$s_{n-2}^{(2)} = s_{n-3}^{(2)} + \alpha \frac{d^2}{dt^2} s_{n-3}^{p_{n-3}/q_{n-3}} + \beta s_{n-3}^{(3)} \tag{20}$$

$$s_{n-3}^{(3)} = s_{n-4}^{(3)} + \alpha \frac{d^3}{dt^3} s_{n-4}^{p_{n-4}/q_{n-4}} + \beta s_{n-4}^{(4)} \tag{21}$$

Then, by taking the derivative of the s_{n-1} by recursive steps according to formula (19), we can get:

$$\begin{aligned} \dot{s}_{n-1} &= \dot{s}_{n-2} + \alpha \frac{d}{dt} s_{n-2}^{p_{n-2}/q_{n-2}} + \beta s_{n-2}^{(2)} \\ &= \dot{s}_{n-2} + \beta s_{n-3}^{(2)} + \beta^2 s_{n-4}^{(3)} + \alpha \frac{d}{dt} s_{n-2}^{p_{n-2}/q_{n-2}} + \alpha\beta \frac{d^2}{dt^2} s_{n-3}^{p_{n-3}/q_{n-3}} + \alpha\beta^2 \frac{d^3}{dt^3} S_{n-4}^{p_{n-4}/q_{n-4}} + \beta^3 s_{n-4}^{(4)} \\ &= \beta^{n-1} s_0^{(n)} + \sum_{k=0}^{n-2} \beta^k s_{n-k-2}^{(k+1)} + \sum_{k=0}^{n-2} \alpha\beta^k \frac{d^{k+1}}{dt^{k+1}} s_{n-k-2}^{p_{n-k-2}/q_{n-k-2}} \end{aligned} \tag{22}$$

3.4.2 | Fractional-order fast fixed-time reaching law

The following fractional-order fast fixed-time reaching law is proposed due to the satisfactory performance:

$$\dot{s}_{n-1} = \frac{1}{\beta^{n-1}} \left[- \left(\phi_1 D^{-\mu_1} s_{n-1}^{\breve{\lambda}} + \phi_2 D^{-\mu_2} s_{n-1}^{\frac{\lambda_3}{\lambda_4}} \right) \right] \tag{23}$$

where $D^{-\mu_1}$ and $D^{-\mu_2}$ are the abbreviated forms of ${}_0D_{s_{n-1}}^{-\mu_1}$ and ${}_0D_{s_{n-1}}^{-\mu_2}$, they are the fractional order operators with the orders $0 < \mu_1 < 1$ and $0 < \mu_2 < 1/2$ those are both the ratio of a positive even to a positive odd number and $\breve{\lambda}$ satisfies the following equation:

$$\breve{\lambda} = \frac{1}{2} + \frac{\lambda_1}{2\lambda_2} + \left(\frac{\lambda_1}{2\lambda_2} - \frac{1}{2}\right) sign(|s_{n-1}| - 1) \tag{24}$$

then we have

$$s_{n-1}^{\breve{\lambda}} = \begin{cases} s_{n-1}^{\lambda_1/\lambda_2} & |s_{n-1}| > 1 \\ s_{n-1} & |s_{n-1}| < 1 \end{cases} \tag{25}$$

It should be note that $\lambda_i\,(i = 1, 2, 3, 4)$ are all constant positive odd number, and $\lambda_1/\lambda_2 > 1, 0 < \lambda_3/\lambda_4 < 1/2$. Obviously, $\breve{\lambda} \geq 1$.

The above-mentioned FO fast fixed-time reaching law (23) has superior dynamical performance, so the control system will have a faster convergence rate. To demonstrate its superiority, it is compared to three other IO convergence laws as follows:

(1) IO finite-time reaching law

$$\dot{s}_{n-1} = -\phi_1 s_{n-1}^{\lambda_1/\lambda_2} - \phi_2 s_{n-1}^{\lambda_3/\lambda_4} - \phi_3 s_{n-1} \tag{26}$$

(2) IO fixed-time reaching law

$$\dot{s}_{n-1} = -\phi_1 s_{n-1}^{\lambda_1/\lambda_2} - \phi_2 s_{n-1}^{\lambda_3/\lambda_4} \tag{27}$$

(3) IO fast fixed-time reaching law

$$\dot{s}_{n-1} = -\phi_1 s_{n-1}^{\breve{\lambda}} - \phi_2 s_{n-1}^{\lambda_3/\lambda_4} \tag{28}$$

After reasonable selection of parameters, the comparison of dynamical performances between the reaching law proposed in this paper and the other three reaching laws are shown in Figure 4. We can see that the proposed FO fast fixed-time reaching law has the fastest convergence rate. Usually, we have the following conclusions: (1) The convergence time of the finite time reaching law is related to the initial value. The larger the initial value is, the longer the convergence time is. So the fixed-time reaching law is a better choice. (2) The fast fixed-time reaching law is faster than the fixed-time convergence law. (3) Fractional order reaching law has more regulating parameters than integer order approach law, and thus the convergence performance will be better if it is well adjusted.

3.4.3 | Control law

Then we define an intermediate variable for simplicity:

$$V_c = \sum_{k=0}^{m} b_k u^{(k)}(t) \tag{29}$$

Then, the controlled plant (13) can be rewritten as

$$y^{(n)}(t) + \sum_{k=0}^{n-1} a_k y^{(k)}(t) + \hat{\Delta}(t) + \tilde{\Delta}(t) = V(t) \tag{30}$$

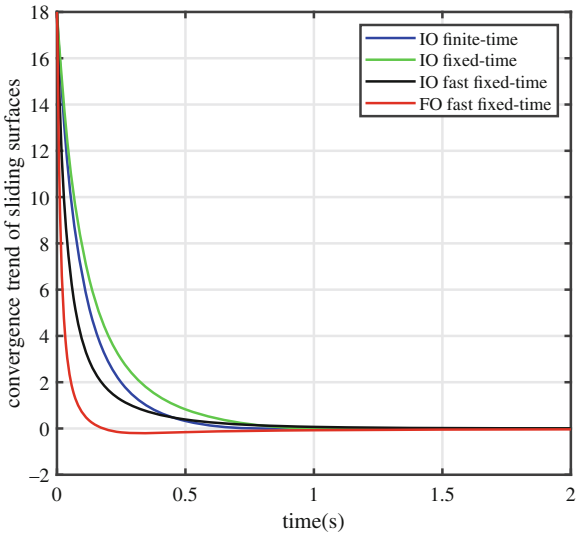

FIGURE 4 Comparison of dynamical performance of the four reaching laws.

Thus, we proposed the following virtual control law:

$$V_c = \frac{1}{\beta^{n-1}}\left[-\left(\phi_2 D^{-\mu} s_{n-1}^{\bar{\lambda}} + \phi_3 D^{-\mu_2} S_{n-1}^{\lambda_1/\lambda_4}\right) - \sum_{k=0}^{n-2}\beta^k S_{n-k-2}^{(k+1)} + \sum_{k=0}^{n-2}\alpha\beta^k \frac{d^{k+1}}{dt^{k+1}} s_{n-k-2}^{p_{n-k-2}/q_{n-k-2}}\right] + y_d^{(n)} + \sum_{k=0}^{n-1} a_k y^{(k)}(t) + \hat{\Delta}(t) \tag{31}$$

Combing (12) and the above control law (31), we can get a robust virtual control law as follows:

$$V_c = \frac{1}{\beta^{n-1}}\left[-\left(\phi_2 D^{-\mu} S_{n-1}^{\lambda} + \phi_3 D^{-\mu_2} S_{n-1}^{\lambda_3/\lambda_4}\right) - \sum_{k=0}^{n-2}\beta^k S_{n-k-2}^{(k+1)} - \sum_{k=0}^{n-2}\alpha\beta^k \frac{d^{k+1}}{dt^{k+1}} S_{n-k-2}^{p_{n-k-2}/q_{n-k-2}}\right] + y_d^{(n)} + \sum_{k=0}^{n-1} a_k y^{(k)}(t) + \sum_{k=0}^{m} b_k u^{(k)}(t-T) - y^{(n)}(t-T) - \sum_{k=0}^{n-1} a_k y^{(k)}(t-T) \tag{32}$$

After the virtual control law V_c is calculated out, we can obtain $u(t)$ from (29). Obviously, V_c is filtered by a filter transfer function $\frac{1}{b_m s^m + b_{m-1}s^{m-1} + \ldots + b_1 s + b_0}$. Thus, the ultimate real control law $u(t)$ can be yielded by the following expression:

$$u = V_c \frac{1}{b_m s^m + b_{m-1}s^{m-1} + \ldots + b_1 s + b_0} \tag{33}$$

The flowchart of our control scheme (33) is illustrated in Figure 2. The stability proof and convergence analysis of the proposed control scheme will be given in the next section.

4 | STABILITY ANALYSIS

Theorem 1. *For controlled plant (11) with tracking error satisfying expression (16), if sliding manifold is designed as (19), the reaching surface is designed as (23), and the robust control law (33) is selected, then the control system is stable. The system states s_{n-1} will convergence from initial state to a small region σ within a fixed settling time T_{reach}.*

where $\sigma = \left\{ s_{n-1} : |s_{n-1}| \le \left(\frac{\beta^{n-1}\tilde{\bar{\Delta}}}{\phi_2 \frac{\Gamma(\lambda_3/\lambda_4+1)}{\Gamma(\mu_2+\lambda_3/\lambda_4+1)}} \right)^{\frac{1}{\lambda_3/\lambda_4+\mu_2}} \right\}$, *and* $T_{reach} < \frac{1}{\phi_1'\left(\breve{\lambda}+\mu_1-1\right)} + \frac{1}{\phi_2'\left(1-\lambda_3/\lambda_4-\mu_2\right)}$.

4.1 | Stability proof

Substituting the perturbance estimation (12) into the controlled plant (30), we can get

$$y^{(n)}(t)+\sum_{k=0}^{n-1}a_k y^{(k)}(t)+\sum_{k=0}^{m}b_k u^{(k)}(t-T)-y^{(n)}(t-T)-\sum_{k=0}^{n-1}a_k y^{(k)}(t-T)+\tilde{\Delta}(t)=V(t) \tag{34}$$

Then, combing the virtual control law (32) and the above controller plant (34), we can get

$$\begin{aligned}&\frac{1}{\beta^{n-1}}\left[-\left(\phi_1 D^{-\mu_1}S_{n-1}^{\bar{\lambda}}+\phi_2 D^{-\mu_2}S_{n-1}^{\lambda_3/\lambda_4}\right)-\sum_{k=0}^{n-2}\beta^k S_{n-k-2}^{(k+1)}-\sum_{k=0}^{n-2}\alpha\beta^k\frac{d^{k+1}}{dt^{k+1}}S_{n-k-2}^{p_{n-k-2}/q_{n-k-2}}\right]\\&=y^{(n)}(t)-y_d^{(n)}+\tilde{\Delta}(t)=e^{(n)}(t)+\tilde{\Delta}(t)=s_0^{(n)}(t)+\tilde{\Delta}(t)\end{aligned} \tag{35}$$

From Equation (22), we have

$$s_0^{(n)}=\frac{1}{\beta^{n-1}}\left[\dot{s}_{n-1}-\sum_{k=0}^{n-2}\beta^k s_{n-k-2}^{(k+1)}-\sum_{k=0}^{n-2}\alpha\beta^k\frac{d^{k+1}}{dt^{k+1}}s_{n-k-2}^{p_{n-k-2}/q_{n-k-2}}\right] \tag{36}$$

Substituting formula (36) into formula (35) and rearranging the formula, we get

$$\dot{s}_{n-1}=-\left(\phi_1 D^{-\mu_1}s_{n-1}^{\breve{\lambda}}+\phi_2 D^{-\mu_2}s_{n-1}^{\lambda_3/\lambda_4}\right)-\beta^{n-1}\tilde{\Delta} \tag{37}$$

Then, a Lyapunov candidate is selected as

$$V=|s_{n-1}| \tag{38}$$

And we have

$$\dot{V}=\dot{s}_{n-1}sign\left(s_{n-1}\right)=\left[-\left(\phi_1 D^{-\mu_1}s_{n-1}^{\breve{\lambda}}+\phi_2 D^{-\mu_2}s_{n-1}^{\lambda_3/\lambda_4}\right)-\beta^{n-1}\tilde{\Delta}\right]sign\left(s_{n-1}\right) \tag{39}$$

Obviously, when $s_{n-1}>0$ we can get

$$\begin{aligned}\dot{V}&=-\phi_1 D^{-\mu_1}s_{n-1}^{\breve{\lambda}}-\phi_2 D^{-\mu_2}s_{n-1}^{\lambda_3/\lambda_4}-\beta^{n-1}\tilde{\Delta}\\&=-\phi_1 D^{-\mu_1}|s_{n-1}|^{\breve{\lambda}}-\phi_2 D^{-\mu_2}|s_{n-1}|^{\lambda_3/\lambda_4}-\beta^{n-1}\tilde{\Delta}\end{aligned} \tag{40}$$

and when $s_{n-1}<0$, because λ_i $(i=1,2,3,4)$ is all odd number, we can obtain the following expression according to **Lemma** 1:

$$\begin{aligned}\dot{V}&=\phi_1 D^{-\mu_1}s_{n-1}^{\breve{\lambda}}+\phi_2 D^{-\mu_2}s_{n-1}^{\lambda_3/\lambda_4}+\beta^{n-1}\tilde{\Delta}\\&=\phi_1 D^{-\mu_1}(-|s_{n-1}|)^{\breve{\lambda}}+\phi_2 D^{-\mu_2}(-|s_{n-1}|)^{\lambda_3/\lambda_4}+\beta^{n-1}\tilde{\Delta}\\&=-\phi_1 D^{-\mu_1}|s_{n-1}|^{\breve{\lambda}}-\phi_2 D^{-\mu_2}|s_{n-1}|^{\lambda_3/\lambda_4}+\beta^{n-1}\tilde{\Delta}\end{aligned} \tag{41}$$

In addition, according to formula (15) we have $\pm\beta^{n-1}\tilde{\Delta}<\beta^{n-1}\bar{\tilde{\Delta}}$. So, we can get

$$\dot{V}<-\phi_1 D^{-\mu_1}|s_{n-1}|^{\breve{\lambda}}-\phi_2 D^{-\mu_2}|s_{n-1}|^{\lambda_3/\lambda_4}+\beta^{n-1}\bar{\tilde{\Delta}} \tag{42}$$

According to **Lemma** 2, we have

$${}_0D_{|s_{n-1}|}^{-\mu_1}|s_{n-1}|^{\breve{\lambda}}=\frac{B(\mu_1,\breve{\lambda}+1)}{\Gamma(\mu_1)}|s_{n-1}|^{\breve{\lambda}+\mu_1} \tag{43}$$

$$ {}_0D_{|s_{n-1}|}^{-\mu_2}|s_{n-1}|^{\lambda_3/\lambda_4} = \frac{B(\mu_2, \lambda_3/\lambda_4+1)}{\Gamma(\mu_2)}|s_{n-1}|^{\lambda_3/\lambda_4+\mu_2} \tag{44} $$

For the purpose of simplifying expression, ${}_0D_{|s_{n-1}|}{}^{-\mu_1}|s_{n-1}|^{\breve{\lambda}}$ in Equation (43) and ${}_0D_{|s_{n-1}|}{}^{-\mu_2}|s_{n-1}|^{\lambda_3/\lambda_4}$ in Equation (44) will be abbreviated as $D^{-\mu_1}|s_{n-1}|^{\breve{\lambda}}$ and $D^{-\mu_2}|s_{n-1}|^{\lambda_3/\lambda_4}$ respectively in subsequent derivation. Then, according to the following definition and attribute of beta function

$$ B(\mu, v) = \int_0^1 t^{\mu-1}(1-t)^{v-1}dt = \frac{\Gamma(\mu)\Gamma(v)}{\Gamma(\mu+v)} \tag{45} $$

Equations (43) and (44) can be re-written as

$$ D^{-\mu_1}|s_{n-1}|^{\breve{\lambda}} = \frac{\Gamma(\breve{\lambda}+1)}{\Gamma(\mu_1+\breve{\lambda}+1)}|s_{n-1}|^{\breve{\lambda}+\mu_1} \tag{46} $$

$$ D^{-\mu_2}|s_{n-1}|^{\lambda_3/\lambda_4} = \frac{\Gamma(\lambda_3/\lambda_4+1)}{\Gamma(\mu_2+\lambda_3/\lambda_4+1)}|s_{n-1}|^{\lambda_3/\lambda_4+\mu_2} \tag{47} $$

Here, it should be pointed out that the value of each gamma function in Equations (46) and (47) is positive because the parameters meet the conditions $\breve{\lambda} \geq 1, 0 < \lambda_3/\lambda_4 < 1/2, 0 < \mu_1 < 1, 0 < \mu_2 < 1/2$.
Substituting (46) and (47) into (42), we can have

$$ \dot{V} < -\phi_1\frac{\Gamma(\breve{\lambda}+1)}{\Gamma(\mu_1+\breve{\lambda}+1)}|s_{n-1}|^{\breve{\lambda}+\mu_1} - \phi_2\frac{\Gamma(\lambda_3/\lambda_4+1)}{\Gamma(\mu_2+\lambda_3/\lambda_4+1)}|s_{n-1}|^{\lambda_3/\lambda_4+\mu_2} + \frac{\beta^{n-1}\bar{\bar{\Delta}}}{|s_{n-1}|^{\lambda_3/\lambda_4+\mu_2}}|s_{n-1}|^{\lambda_3/\lambda_4+\mu_2} \tag{48} $$

Then we define two new variables ϕ_1' and ϕ_2', and they satisfy the following equation relationships

$$ \phi_1' = \phi_1\frac{\Gamma(\breve{\lambda}+1)}{\Gamma(\mu_1+\breve{\lambda}+1)} \tag{49} $$

$$ \phi_2' = \phi_2\frac{\Gamma(\lambda_3/\lambda_4+1)}{\Gamma(\mu_2+\lambda_3/\lambda_4+1)} - \frac{\beta^{n-1}\bar{\bar{\Delta}}}{|s_{n-1}|^{\lambda_3/\lambda_4+\mu_2}} \tag{50} $$

By substituting (49) and (50) into (48), we can get

$$ \dot{V} < -\phi_1'|s_{n-1}|^{\breve{\lambda}+\mu_1} - \phi_2'|s_{n-1}|^{\lambda_3/\lambda_4+\mu_2} \tag{51} $$

Obviously, we can get $\dot{V} < 0$ if $\phi_1' > 0$ and $\phi_2' > 0$. In fact, ϕ_1' is always positive according to (49) and the range of the value of the selected parameters. In addition, the first term in Equation (50) can be very big positive and the second term is a very small positive number. Then $\phi_2' > 0$ holds if appropriate parameters are chosen. Thus, we are able to get

$$ \dot{V} < 0 \tag{52} $$

So, the system state s_{n-1} is reachable, and then the system stability is proved.

4.2 | Convergence region of states s_{n-1}

Let $\phi_2' > 0$ and according to formula (50), we have

$$ |s_{n-1}| > \left(\frac{\beta^{n-1}\bar{\bar{\Delta}}}{\phi_2\frac{\Gamma(\lambda_3/\lambda_4+1)}{\Gamma(\mu_2+\lambda_3/\lambda_4+1)}}\right)^{\frac{1}{\lambda_3/\lambda_4+\mu_2}} \tag{53} $$

The above Equation (53) shows the range that the system state can achieve. It means, system state s_{n-1} will eventually convergence from initial state to the following region:

$$\sigma = \left\{ s_{n-1} : |s_{n-1}| \leq \left(\frac{\rho^{n-1}\bar{\bar{\Delta}}}{\phi_2 \frac{\Gamma(\lambda_3/\lambda_4+1)}{\Gamma(\mu_2+\lambda_3/\lambda_4+1)}} \right)^{\frac{1}{\lambda_3/\lambda_4+\mu_2}} \right\} \tag{54}$$

From the above expression, we can see the convergence region σ is related to the upper bound $\bar{\bar{\Delta}}$ of the estimation error of disturbance. If the $\bar{\bar{\Delta}}$ is set small enough, the system state s_{n-1} will converge to a small enough region.

4.3 | The calculation of settling time

Substituting (38) to (51), we get

$$\dot{V} < -\phi_1' V^{\breve{\lambda}+\mu_1} - \phi_2' V^{\lambda_3/\lambda_4+\mu_2} \tag{55}$$

Here, we can see that each parameter in formula (55) meets the requirements in **Lemma** 3. This is because $\breve{\lambda} \geq 1$, $0 < \lambda_3/\lambda_4 < 1/2$, $0 < \mu_1 < 1$ is the ratio of a positive even to a positive odd number, $0 < \mu_2 < 1/2$ is the ratio of a positive even to a positive odd number. Then, we can get $\breve{\lambda} + \mu_1 > 1$, $\lambda_3/\lambda_4 + \mu_2 < 1$. According to **Lemma** 3, the settling time of the system state can be obtained as follows:

$$T_{reach} < \frac{1}{\phi_1'\left(\breve{\lambda}+\mu_1-1\right)} + \frac{1}{\phi_2'(1-\lambda_3/\lambda_4-\mu_2)} \tag{56}$$

5 | EXPERIMENTAL RESULTS

To demonstrate the clear performance benefits furnished by the proposed control scheme, a battery of careful, comparative experiments were performed. Their details, results and relevant discussions are presented here.

5.1 | Experimental settings and tuning of controller parameters

The control objective is to track triangular trajectories accurately. Extensive simulations were carried out on the identified model of the nanopositioner axis. The experimental setup employed in this paper is shown in Figure 1A. A PCI-6621 data acquisition card from National Instruments installed on a PC running the Real-Time Module from LabVIEW is used to interface between the experimental platform and the control design. The PC utilized is an OPTIPLEX 780 with an Intel(R) Core(TM)2 Duo Processor running at 3.167 GHz and equipped with 2 GB of DDR3 RAM memory. The cross-coupling between the two axes was measured to be −40 dB; small enough to be neglected, thereby making it feasible to treat each axis as being decoupled from the other. Throughout the experiments, the unused axis has its input terminals shorted in order to avoid spurious excitation. The sampling frequency of the A/D and D/A converters of the control system is set to 20 kHz.

The choice of controller parameters affects the tracking performance of the system. In convergence phase, Equation (23) indicates that the performance of the system is determined by parameters $\phi_1, \phi_2, \mu_1, \mu_2, \lambda_1, \lambda_2, \lambda_3, \lambda_4$. In sliding phase, Equation (19) indicates that the performance of the system is determined by parameters α, β, p_j, q_j. Constrained by the sliding Equation (19), both α and β have to be a small value because the errors are small. α controls the stage far away from the equilibrium. And the smaller its value, the higher the bandwidth.If the value is too large, the convergence time will increase. β controls the near equilibrium stage. And the smaller its value, the higher the bandwidth. If the value is too small, the convergence time will increase. If the value is too large, it can even lead to instability. p_j and

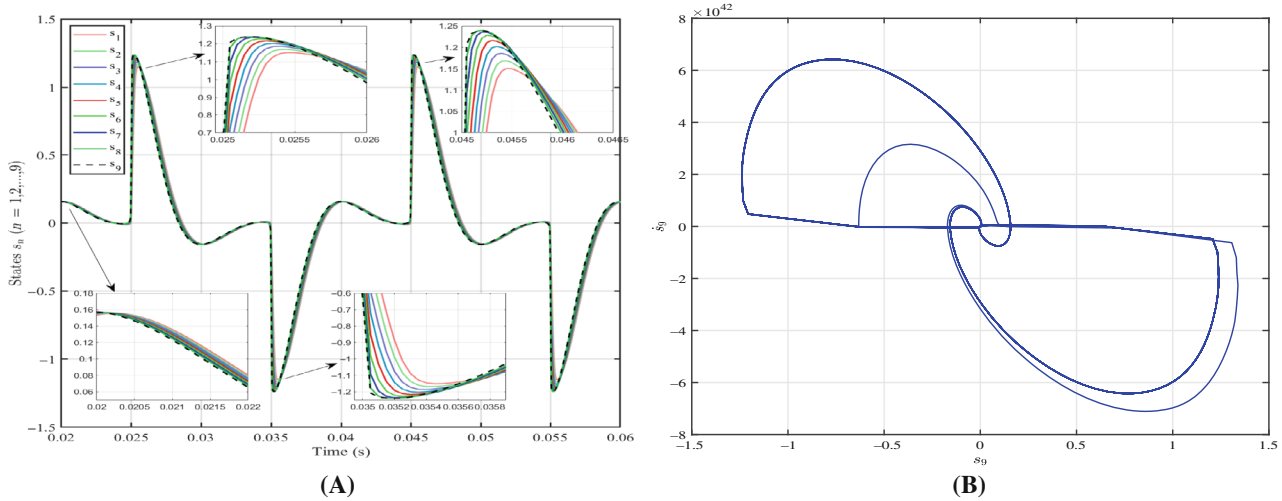

FIGURE 5 (A) The evolution of state variables versus time. (B) phase-plane portrait for a triangular trajectory, demonstrating the proposed controller's convergence property.

q_j are all odd numbers; the ratio between p_j to q_j has to be at least greater than $n-1-j$ to ensure the non-singularity property. A numerical search was employed to aid in selection of the appropriate controller parameters. The resulting controller parameters are as follows:

1. $\alpha = 0.005, \beta = 0.000035$
2. $p_0 = 129, p_1 = 115, p_2 = 103, p_3 = 89, p_4 = 77, p_5 = 63, p_6 = 51, p_7 = 37, p_8 = 25$
3. $q_0 = 13, q_1 = 13, q_2 = 13, q_3 = 13, q_4 = 13, q_5 = 13, q_6 = 13, q_7 = 13, q_8 = 13$
4. $\phi_1 = 820, \phi_2 = 40$
5. $\mu_1 = 6/115, \mu_2 = 4/115$
6. $\lambda_1 = 5, \lambda_2 = 3, \lambda_3 = 3, \lambda_4 = 7$

5.2 | Analysis of phase trajectories

Here, the phase trajectories under the above selected parameters are given and discussed. It should be noted that as the controller parameters change, the controller performance and phase trajectory will also change, but the trends are consistent. Figure 5A shows the state variables of s_n $(n = 1, 2, \ldots, 9)$. Figure 5B shows the phase plane between $\dot{s}_9$ and s_9. We can see that the $\dot{s}_9$ can convergence very steeply, and can even convergence to equilibrium very quickly at each discontinuous point of the triangular wave. And then, s_9 will convergence to a small neighborhood of zero, and $s_8, s_7, s_6, \ldots, s_1$ will sequentially converge to equilibrium according to the law given in Equation (19), as shown in Figure 5A. When convergence law approaches zero, s_9 will reach equilibrium point. And then $(s_9, s_8, s_7, \ldots, s_1)$ will converge to equilibrium point sequentially. Then, $s_0 (= e = y - y_d)$ will also reach equilibrium point. All the states s_n $(n = 1, 2, \ldots 9)$ satisfies the similar convergence law, shown in Equation (19).

5.3 | Comparative analysis of tracking performance

In order to compare the tracking performance of different controllers quantitatively, some error indicators must be defined in advance. In this work, the following percent maximum (MAX) error and root mean squared (RMS) error are employed for quantitative evaluation:

$$e_{rms}(\%) = \left(\frac{\sqrt{\frac{1}{N}\sum_{i=1}^{N} e_i^2}}{\max(y_d) - \min(y_d)} \right) \times 100\% \tag{57}$$

$$e_{\max}(\%) = \frac{\max(|e|)}{\max(y_d) - \min(y_d)} \times 100\% \tag{58}$$

where $e = y - y_d$ is the error, N is the number of data sets, y_d is the reference position.

To verify the positioning performance of the proposed SMC controller, triangular trajectories with fundamental frequencies of 25, 50, and 100 Hz were chosen in the experiments. To compare the positioning performance of the proposed controller, it was compared with three suitably designed controllers that have emerged as benchmark schemes over the years. The first scheme is a simple PID controller. The individual gains are tuned to results in maximum positioning bandwidth using the full high-order model. The transfer function for the designed PID controller is given by $C_{PID} = 1.5 + \frac{6500}{s} + 0.0005s$. The second control scheme is the popularly employed combination of damping and traking actions where an inner-loop damping controller is implemented in tandem with a tracking controller in the outer loop.[64] Due to its popularity and excellent performance, the positive position feedback (PPF) damping controller combined with an integral (I) tracking controller was employed. the transfer function for the designed PPF damping controller is given by: $C_{PPF} = \frac{6.320\times10^7}{s^2+11740s+4.855\times10^7}$ and the corresponding integral gain $K_I = 1494$. The third control scheme is a fully tuned conventional linear high-order sliding mode control (LSMC) scheme,[65] employed to achieve a relatively fair contrast and modified with equivalent and switching actions to deal with this high-order plant. The designed sliding mode surface is in the form of $\sum_{i=0}^{9} c_i e^{(i)}$, and the switching action is $2s + 0.05\text{sign}(s)$. The comparison of the time-domain tracking results are presented in Figure 6. In addition, Table 1 shows the quantitative comparison of performance for triangular trajectory tracking between the proposed controller against the PID, PPF+I, and LSMC control strategies. Obviously, the MAX and RMS errors of the proposed controller are significantly reduced compared with PPF+I, PID, and LSMC controller. This means that the performance of the proposed controller is greatly improved. From Figure 6, the following advantages of the proposed controller can also be shown: (1) the high tracking precision thanks to the chattering-free property; (2) fast convergence guaranteed by the fast terminal sliding manifold and fractional-order fixed-time reaching law.

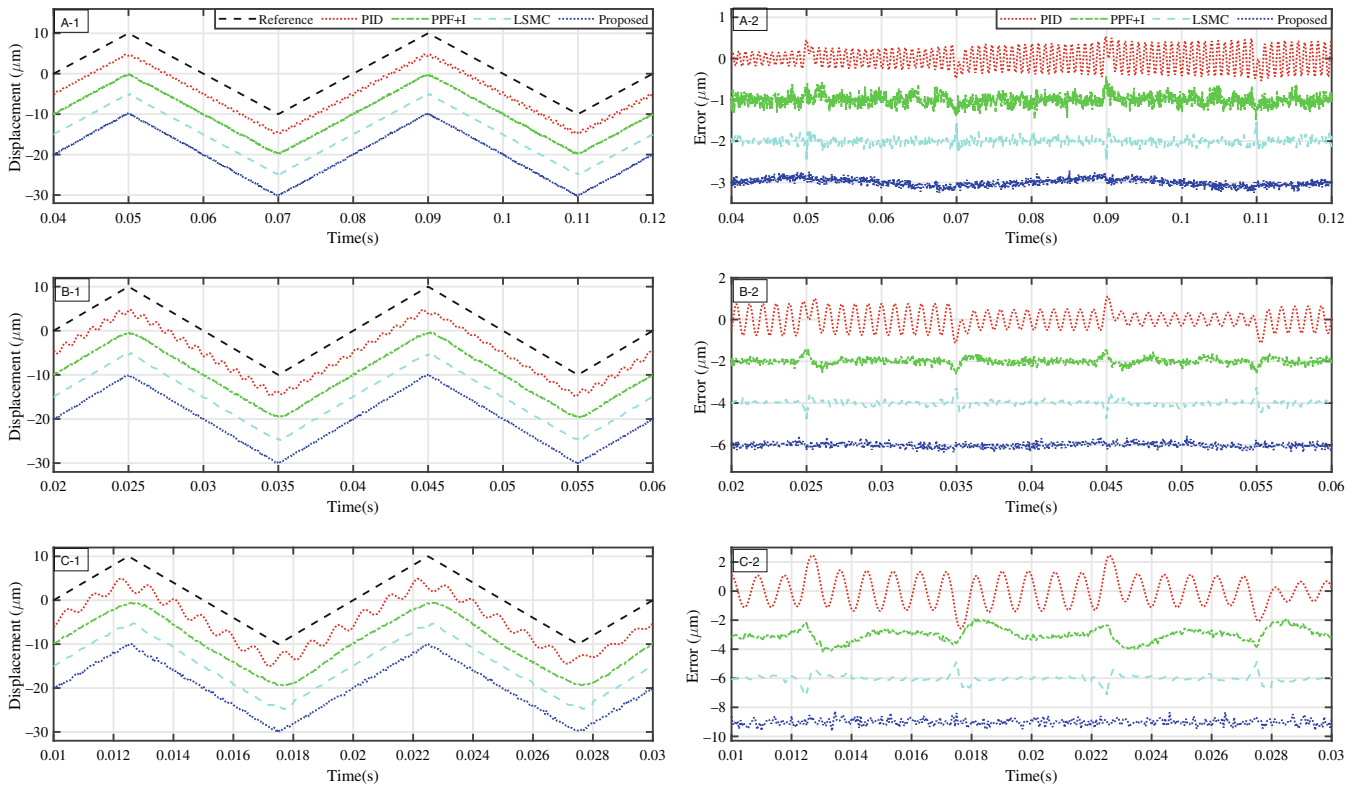

FIGURE 6 Closed-loop time-domain tracking results for 25, 50, and 100 Hz triangular reference inputs (A-1, B-1, and C-1). For clarity, the traces are offset by 5 μ m. The corresponding tracking errors are plotted in (A-2, B-2, and C-2). These errors are also offset adequately, for clarity.

TABLE 1 Triangular wave tracking errors of the 4 controllers

Error (%)	Frequency	PID	PPF+I	LSMC	Proposed
MAX	25 Hz	3.40	1.94	1.84	1.15
	50 Hz	6.38	3.35	3.26	2.16
	100 Hz	13.35	5.12	5.05	2.34
RMS	25 Hz	1.05	0.37	0.35	0.31
	50 Hz	2.43	0.64	0.60	0.51
	100 Hz	4.46	2.29	2.23	1.54

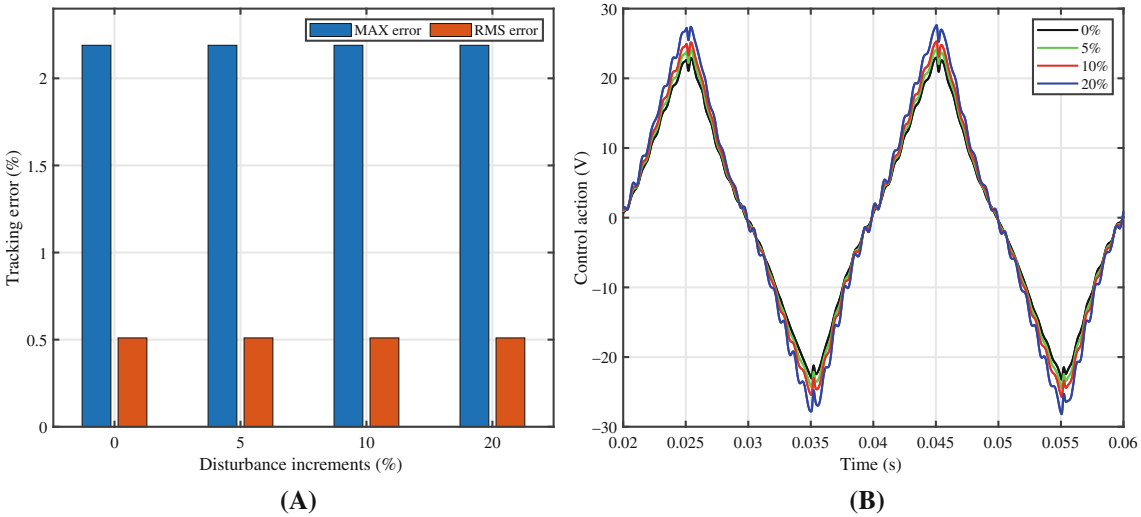

FIGURE 7 Results of robustness when tracking a 50 Hz reference command for 0%, 5%, 10%, 20% disturbance increments. (A) MAX and RMS tracking errors. (B) Steady state control actions.

5.4 | Robustness analysis

In this section, the robustness of the proposed controller is verified by changing the values of the disturbance when tracking a 50 Hz triangular wave trajectory. The disturbance increments are equivalent to the changes in the frequency and damping of the dominant first resonant mode. In each experiment, the disturbance increment is set to 0%, 5%, 10%, 20%, respectively. And the corresponding steady-state tracking errors and control actions are shown in Figure 7A,B. We can see that the MAX and RMS tracking errors basically keep the same as the increase of the disturbances. And the control action changes in terms of amplitude and ripple with the increase of the disturbances. Thus, the robustness of the proposed control method against the disturbances can be verified. This property comes from the robustness of the sliding manifold and the TDE estimator.

6 | CONCLUSIONS

A new robust fractional-order fast terminal sliding model control approach with high-order sliding model dynamics has been presented for a piezoelectric platform in this paper. With the well established accurate model of the controlled plant, controller is synthesized with the aid of *Inverse model of hysteresis*, *TDE disturbance estimation*, and *Sliding mode based control design*. The recursive high-order sliding manifold and fractional-order fast fixed-time reaching law can guarantee a faster response and fixed convergence time while avoiding potential singularity and chattering problems. The stability of the proposed scheme has been proved via the Lyapunov framework. The convergence region and the settling time of system state have also been analyzed theoretically. The excellent performances of the proposed controller have been

verified by comparing the experimental results with PID, PPF+I, LSMC controllers. The proposed control method has been proved to have many superior performances in terms of high tracking accuracy, fast convergence, non-singularity, robustness.

ACKNOWLEDGMENTS

This work is supported by the China Scholarship Council under grant no. 201908410107 and by the National Natural Science Foundation of China under grant no. 51505133. The authors also thank the anonymous reviewers for their insightful and constructive comments.

CONFLICT OF INTEREST

The authors declare that they have no known competing financial interests or personal relationships that could have appeared to influence the work reported in this paper.

DATA AVAILABILITY STATEMENT

All the codes presented in this manuscript can be furnished on reasonable requests to the corresponding author.

ORCID

Geng Wang https://orcid.org/0000-0002-6876-3317

REFERENCES

1. Li L, Li CX, Gu G, Zhu L. Modified repetitive control based cross-coupling compensation approach for the piezoelectric tube scanner of atomic force microscopes. *IEEE/ASME Trans Mechatron*. 2019;24(2):666-676.
2. Angelov T, Ahmad A, Guliyev E, et al. Six-axis AFM in SEM with self-sensing and self-transduced cantilever for high speed analysis and nanolithography. *J Vac Sci Technol B, Nanotechnol Microelectron Mater Process Meas Phenom*. 2016;34(6):06KB01.
3. Shengdong Yu MX, Lin H, Ma J. Precise robust motion control of cell puncture mechanism driven by piezoelectric actuators with fractional-order nonsingular terminal sliding mode control. *Bio-des. Manuf.* 2020;3:410-426.
4. Zhao D, Zhu Z, Huang P, Guo P, Zhu L, Zhu Z. Development of a piezoelectrically actuated dual-stage fast tool servo. *Mech. Syst. Signal Process.* 2020;144:144. doi:10.1016/j.ymssp.2020.106873
5. Gu GY, Zhu LM, Su CY, Ding H, Fatikow S. Modeling and control of piezo-actuated nanopositioning stages: a survey. *IEEE Trans Autom Sci Eng*. 2014;13(1):313-332.
6. Sabarianand D, Karthikeyan P, Muthuramalingam T. A review on control strategies for compensation of hysteresis and creep on piezoelectric actuators based micro systems. *Mech. Syst. Signal Process.* 2020;49(1-2):140. doi:10.1016/j.ymssp.2020.106634
7. Hassani V, Tjahjowidodo T, Do TN. A survey on hysteresis modeling, identification and control. *Mech. Syst. Signal Process.* 2014;49(1-2):209-233.
8. Wang G, Chen G, Zhou H, Bai F. Modeling and tracking control for piezoelectric actuator based on a new asymmetric hysteresis model. *IEEE/CAA J Autom Sin*. 2017;4(4):782-791. doi:10.1109/JAS.2016.7510136
9. Bi S, Wang L, Wen S, Deng M. Operator-based robust nonlinear control for SISO and MIMO nonlinear systems with PI hysteresis. *IEEE/CAA J Autom Sin*. 2018;5(2):523-530. doi:10.1109/JAS.2016.7510175
10. Kang S, Wu H, Yang X, Li Y, Wang Y. Fractional-order robust model reference adaptive control of piezo-actuated active vibration isolation systems using output feedback and multi-objective optimization algorithm. *J Vib Control*. 2020;26(1-2):19-35.
11. Li K, Yang Z, Lallart M, Zhou S, Chen Y, Liu H. Hybrid hysteresis modeling and inverse model compensation of piezoelectric actuators. *Smart Mater Struct*. 2019;28(11):115038.
12. Junior WRL, Martins SA, Nepomuceno EG, Lacerda MJ. Control of hysteretic systems through an analytical inverse compensation based on a NARX model. *IEEE Access*. 2019;7:98228-98237.
13. Zhang Q, Dong Y, Peng Y, Luo J, Xie S, Pu H. Asymmetric Bouc–Wen hysteresis modeling and inverse compensation for piezoelectric actuator via a genetic algorithm–based particle swarm optimization identification algorithm. *J Intell Mater Syst Struct*. 2019;30(8):1263-1275.
14. Kaci A, Giraud-Audine C, Giraud F, Amberg M, Lemaire-Semail B. LQR based MIMO-PID controller for the vector control of an underdamped harmonic oscillator. *Mech. Syst. Signal Process.* 2019;13(14):134. doi:10.1016/j.ymssp.2019.106314
15. Zhang Y, Yan P. Adaptive observer-based integral sliding mode control of a piezoelectric nano-manipulator. *IET Control Theory Appl*. 2019;13(14):2173-2180.
16. Zhang L, Xu S, Ju X, Cui N. Flexible satellite control via fixed-time prescribed performance control and fully adaptive component synthesis vibration suppression. *Nonlinear Dyn*. 2020;100(4):3413-3432.
17. Xie S, Ren J. High-speed AFM imaging via iterative learning-based model predictive control. *Mechatron*. 2019;57:86-94.
18. Feng Z, Liang W, Ling J, Xiao X, Tan KK, Lee TH. Integral terminal sliding-mode-based adaptive integral backstepping control for precision motion of a piezoelectric ultrasonic motor. *Mech. Syst. Signal Process.* 2020;144:144. doi:10.1016/j.ymssp.2020.106856
19. Sun Z, Zheng J, Man Z, Fu M, Lu R. Nested adaptive super-twisting sliding mode control design for a vehicle steer-by-wire system. *Mech. Syst. Signal Process.* 2019;122:658-672. doi:10.1016/j.ymssp.2018.12.050

20. Liu K, Cao Y, Wang S, Li Y. Terminal sliding mode control for landing on asteroids based on double power reaching law. Paper presented at: IEEE; 2015; 2444–2449.
21. Park KB, Tsuji T. Terminal sliding mode control of second-order nonlinear uncertain systems. *Int J Robust Nonlinear Control: IFAC-Affiliated J*. 1999;9(11):769-780.
22. Zhao X, Shi P, Zheng X. Fuzzy adaptive control design and discretization for a class of nonlinear uncertain systems. *IEEE Trans Cybern*. 2015;46(6):1476-1483.
23. Chang XH, Yang GH. New results on output feedback $H_{infinity}$ control for linear discrete-time systems. *IEEE Trans Automat Control*. 2013;59(5):1355-1359.
24. Zhang R, Zeng D, Zhong S, Yu Y. Event-triggered sampling control for stability and stabilization of memristive neural networks with communication delays. *Appl Math Comput*. 2017;310:57-74.
25. Chang XH, Wang YM. Peak-to-peak filtering for networked nonlinear DC motor systems with quantization. *IEEE Trans Industr Inform*. 2018;14(12):5378-5388.
26. Zhang R, Liu X, Zeng D, Zhong S, Shi K. A novel approach to stability and stabilization of fuzzy sampled-data Markovian chaotic systems. *Fuzzy Sets Syst*. 2018;344:108-128.
27. Park JH, Shen H, Chang XH, Lee TH. *Fuzzy Resilient Energy-to-Peak Filter Design for Continuous-Time Nonlinear Systems*. Springer; 2019:119-139.
28. He S, Song J. Finite-time sliding mode control design for a class of uncertain conic nonlinear systems. *IEEE/CAA J Autom Sin*. 2017;4(4):809-816. doi:10.1109/JAS.2017.7510643
29. Feng Y, Yu X, Man Z. Non-singular terminal sliding mode control of rigid manipulators. *Automatica*. 2002;38(12):2159-2167.
30. Al-Ghanimi A, Zheng J, Man Z. Robust and fast non-singular terminal sliding mode control for piezoelectric actuators. *IET Control Theory Appl*. 2015;9(18):2678-2687.
31. Yang L, Yang J. Nonsingular fast terminal sliding-mode control for nonlinear dynamical systems. *Int J Robust Nonlinear Control*. 2011;21(16):1865-1879.
32. Yu S, Yu X, Shirinzadeh B, Man Z. Continuous finite-time control for robotic manipulators with terminal sliding mode. *Automatica*. 2005;41(11):1957-1964.
33. Wang B, Shi K, Yang L, Wu F, Chen D. Fuzzy generalised predictive control for a class of fractional-order non-linear systems. *IET Control Theory Appl*. 2017;12(1):87-96.
34. Wang B, Xue J, Wu F, Zhu D. Finite time takagi-sugeno fuzzy control for hydro-turbine governing system. *J Vib Control*. 2018;24(5):1001-1010.
35. Aghababa MP, Aghababa HP. Finite-time stabilization of non-autonomous uncertain chaotic centrifugal flywheel governor systems with input nonlinearities. *J Vib Control*. 2014;20(3):436-446.
36. Ning B, Han QL, Zuo Z. Distributed optimization for multiagent systems: An edge-based fixed-time consensus approach. *IEEE Trans Cybern*. 2017;49(1):122-132.
37. Zhu Z, To S, Li Y, Zhu WL, Bian L. External force estimation of a piezo-actuated compliant mechanism based on a fractional order hysteresis model. *Mech. Syst. Signal Process.* 2018;110:296-306. doi:10.1016/j.ymssp.2018.03.012
38. Tuan LA. Fractional-order fast terminal back-stepping sliding mode control of crawler cranes. *Mech Mach Theory*. 2019;137:297-314. doi:10.1016/j.mechmachtheory.2019.03.027
39. Le AT. Neural Observer and Adaptive Fractional-Order Back-Stepping Fast Terminal Sliding Mode Control of RTG Cranes. *IEEE Trans Ind Electron*. 2020;99:1.
40. Xu R, Pan W, Zea W. High-precision tracking control of a piezoelectric micro-nano platform using sliding mode control with the fractional-order operator. *Int. J. Precis. Eng. Manuf.* 2020;21:2277-2286.
41. Shirkavand M, Pourgholi M. Robust fixed-time synchronization of fractional order chaotic using free chattering nonsingular adaptive fractional sliding mode controller design. *Chaos Solit Fractals*. 2018;113:135-147.
42. Van Trieu P, Cuong HM, Dong HQ, Tuan NH, Tuan LA. Adaptive fractional-order fast terminal sliding mode with fault-tolerant control for underactuated mechanical systems: application to tower cranes. *Autom Constr*. 2021;123:103533. doi:10.1016/j.autcon.2020.103533
43. Cuong HM, Dong HQ, Trieu PV, Tuan LA. Adaptive fractional-order terminal sliding mode control of rubber-tired gantry cranes with uncertainties and unknown disturbances. *Mech Syst Signal Process*. 2021;154:107601. doi:10.1016/j.ymssp.2020.107601
44. Shao S, Chen M. Fractional-order control for a novel chaotic system without equilibrium. *IEEE/CAA J Autom Sin*. 2019;6(4):1000-1009. doi:10.1109/JAS.2016.7510124
45. Yin C, Cheng Y, Chen Y, Stark B, Zhong S. Adaptive fractional-order switching-type control method design for 3D fractional-order nonlinear systems. *Nonlinear Dyn*. 2015;82(1-2):39-52.
46. Hu R, Deng H, Zhang Y. Novel dynamic-sliding-mode-manifold-based continuous fractional-order nonsingular terminal sliding mode control for a class of second-order nonlinear systems. *IEEE Access*. 2020;8:19820-19829. doi:10.1109/ACCESS.2020.2968558
47. Gao P, Zhang G, Ouyang H, Mei L. An adaptive super twisting nonlinear fractional order PID sliding mode control of permanent magnet synchronous motor speed regulation system based on extended state observer. *IEEE Access*. 2020;8:53498-53510. doi:10.1109/ACCESS.2020.2980390
48. Huang S, Wang J. Fixed-time fractional-order sliding mode control for nonlinear power systems. *J Vib Control*. 2020;26(17-18):1425-1434. doi:10.1177/1077546319898311
49. Ni J, Liu L, Liu C, Hu X, Li S. Fast fixed-time nonsingular terminal sliding mode control and its application to chaos suppression in power system. *IEEE Trans Circuits Syst II: Express Briefs*. 2017;64(2):151-155. doi:10.1109/TCSII.2016.2551539

50. Yu S, Feng Y, Yang X. Extended state observer–based fractional order sliding-mode control of piezoelectric actuators. *Proc Inst Mech Eng I: J Syst Control Eng*. 2021;235(1):39-51.
51. Zhang S, Li Z, Wang HN, Xiong T. Fractional order sliding mode control based on single parameter adaptive law for nano-positioning of piezoelectric actuators. *IET Control Theory Appl*. 2021;15(10):1422-1437.
52. Wang Z, Zhang Z, Mao J. Precision tracking control of piezoelectric actuator based on Bouc-Wen hysteresis compensator. *Electron Lett*. 2012;48(23):1459-1460.
53. Matignon D. Stability results for fractional differential equations with applications to control processing. *Comput Eng Syst Appl*. 1996;2:963-968.
54. Monje CA, Chen Y, Vinagre BM, Xue D, Feliu-Batlle V. *Fractional-Order Systems and Controls: Fundamentals and Applications*. Springer Science & Business Media; 2010.
55. Kilbas A, Srivastava HM, Trujillo JJ. *Theory and Applications of Fractional Differential Equations*. Vol 204. Elsevier; 2006.
56. Zuo Z, Tie L. Distributed robust finite-time nonlinear consensus protocols for multi-agent systems. *Int J Syst Sci*. 2016;47(6):1366-1375.
57. Xue D, Zhao C, Chen Y. A modified approximation method of fractional order system. Paper presented at: IEEE; 2006; 1043–1048.
58. Rakotondrabe M. Bouc–Wen modeling and inverse multiplicative structure to compensate hysteresis nonlinearity in piezoelectric actuators. *IEEE Trans Autom Sci Eng*. 2010;8(2):428-431.
59. Wang G, Chen G, Bai F. Modeling and identification of asymmetric Bouc–Wen hysteresis for piezoelectric actuator via a novel differential evolution algorithm. *Sens Actuators A Phys*. 2015;235:105-118. doi:10.1016/j.sna.2015.09.043
60. Minggang G, Zhi Q, Yanlong LI. Sliding mode control with perturbation estimation and hysteresis compensator based on Bouc-Wen model in tackling fast-varying sinusoidal position control of a piezoelectric actuator. *J Syst Sci Complex*. 2016;29:367-381.
61. Wang Y, Zhu K, Chen B, Jin M. Model-free continuous nonsingular fast terminal sliding mode control for cable-driven manipulators. *ISA Trans*. 2020;98:483-495. doi:10.1016/j.isatra.2019.08.046
62. Sun G, Ma Z. Practical tracking control of linear motor with adaptive fractional order terminal sliding mode control. *IEEE/ASME Trans Mechatron*. 2017;22(6):2643-2653. doi:10.1109/TMECH.2017.2766279
63. Xiong L, Li P, Ma M, Wang Z, Wang J. Output power quality enhancement of PMSG with fractional order sliding mode control. *Int J Electr Power Energy Syst*. 2020;115:105402. doi:10.1016/j.ijepes.2019.105402
64. Moon RJ, San-Millan A, Aleyaasin M, Feliu V, Aphale SS. *Selection of Positive Position Feedback Controllers for Damping and Precision Positioning Applications*. Springer; 2017:289-301.
65. Levant A. Higher-order sliding modes, differentiation and output-feedback control. *Int J Control*. 2003;76(9-10):924-941.

How to cite this article: Wang G, Zhou Y, Ni L, Aphale SS. Robust fractional-order fast terminal sliding mode control with fixed-time reaching law for high-performance nanopositioning. *Int J Robust Nonlinear Control*. 2023;33(4):2596-2614. doi: 10.1002/rnc.6526